Assessment of a BEMT-based rotor aerodynamic model under uniform aligned steady inflow

Boatto, U.; Bonnet, Jean-Paul; Avallone, F.; Ragni, D.

DOI
10.2514/6.2023-0609

Publication date
2023

Document Version
Final published version

Published in
AIAA SciTech Forum 2023

AIAA SciTech Forum
23-27 January 2023, National Harbor, MD & Online
AIAA SCITECH 2023 Forum

10.2514/6.2023-0609

Assessment of a BEMT-based rotor aerodynamic model under uniform aligned steady inflow

Umberto Boatto*, Paul Bonnet†, Francesco Avallone‡, Daniele Ragni§

The design of efficient rotor blades is affected by the accuracy of aerodynamic prediction methods for load distributions and power computations. Research showed that the accuracy of BEMT-based industrial codes decreases at high inflow-speed under uniform aligned steady conditions. The identified reasons are inaccuracies in the semi-empirical corrections for 3D effects such as stall delay and tip-losses. This study scrutinizes such corrections by comparison with URANS CFD simulations. Results confirm that the accuracy of the rotor thrust and power coefficients reduces up to 30% for a tip speed ratio of 4. The identified causes in the inboard blade are: (1) a more than twice as large drag coefficient given by the Eggers stall delay correction, (2) a 20% loading overestimation due to the unaccounted root-vortex downwash. Furthermore, the linear interpolation between the cylinder and the DU40 airfoil polars near the root as well as the modeling of 2D separation affect the accuracy at least as much as the stall delay correction at a tip speed ratio of 4. Next, the inadequacy of the Prandtl tip-loss factor at a tip speed ratio of 10 provides 5 to 15% higher loads in the outboard blade. It is recommended to extend stall delay corrections or tune the Prandtl root-loss correction to the location of the maximum chord to capture the root-vortex downwash effect, as the phenomenon is observed on the CFD-extracted lift polar and blade flow streamlines. Finally, 2D RANS simulations of the inboard blade profiles should be compared with the 3D ones from the rotating blade to isolate the effect of stall delay on the pressure and skin friction coefficient distributions to further address the modeling of the drag coefficient.

I. Nomenclature

c, r	=	blade profile chord length (m) and radial location (m)
D, R	=	rotor diameter and radius (m)
λ	=	tip speed ratio (-)
U	=	inflow speed (m/s)
Ω	=	rotor speed (rpm)
ρ	=	fluid flow density (kg/m^3)
$\bar{a}$, a_B	=	annular-averaged and local axial induction factor (-)
$\bar{a'}$, a'_B	=	annular-averaged and local tangential induction factor (-)
$\bar{\alpha}$, α_B, α_W	=	annular-averaged, local, and downwash angle of attack (deg)
F_A, F_T	=	out-of-plane (axial) and in-plane (tangential) force densities (N/m)
c_l, c_d	=	lift and drag coefficients (-)
ϕ, θ	=	blade profile inflow and twist angles (deg)
c_p	=	pressure coefficient (-)
c_{f_c}, c_{f_r}	=	chordwise and radial skin-friction coefficients (-)
C_T, C_P	=	annular thrust and annular power coefficients (-)

*Marie Curie Early-Stage Researcher, Siemens Digital Industry Software N.V., Rue des Chasseurs Ardennais 8, Angleur, 4031, Belgium.
†FEA Solver Development Aero-hydro-servo-elasticity, Siemens Digital Industry Software S.L.U., C/Lluis Muntadas número 5, 08940 Cornellá de Llobregat (Barcelona), Spain.
‡Assistant Professor, Delft University of Technology, AWEP Department, Kluyverweg 1, 2629 HS Delft, The Netherlands.
§Associate Professor, Delft University of Technology, AWEP Department, Kluyverweg 1, 2629 HS Delft, The Netherlands.

II. Introduction

Wind energy is a relevant and mature technology in electric power production as a result of decades of technical developments, especially on the rotor blades [1, 2]. The design of efficient rotor blades requires accurate, robust, and reasonably fast aerodynamic prediction methods to estimate their power output and wind-induced load distributions [3–5].

Industrial prediction methods consist of low-fidelity engineering methods such as the Blade Element Momentum Theory (BEMT) [6] extended with semi-empirical corrections [3, 7, 8]. Considerable efforts were made in the past to compare BEMT-based codes with 3D RANS simulations and wind tunnel experiments [4, 9, 10]. Engineering methods failed to accurately predict the rotor loads distributions under uniform, aligned, steady inflow, particularly at high inflow speed. In the NREL blind comparison [9], BEMT-based codes overpredicted by 10 to 40% the experimental outboard blade loading due to inaccuracies in Tip-Loss (TL) corrections and underpredicted the normal inboard force by more than 100% at high wind speed due to 2D airfoil data, while CFD codes provided a more favorable match under stall. In the Mexnext Phase I project [4], BEMT-based codes underpredicted by 20% the experimental and CFD normal force at above-rated conditions, despite Stall Delay (SD) corrections, and overestimated the outboard loads at all inflow speeds by an average of 15%. In Phase III [10], it was confirmed that the most significant deviations between BEMT and CFD loads were in the tip region. Therefore, BEMT-based codes do not accurately predict the rotor load distributions due to the limitations in the corrections for 3D aerodynamic phenomena such as TL and SD, at least under idealized inflow conditions.

Concerning the outboard blade, most industrial BEMT codes employ variations of the Prandtl [11] Tip and Root-Loss (TRL) factor in improving the accuracy of the outboard blade loads and power [12]. The original Prandtl model was derived by assuming a constant blade bound circulation with concentrated trailing vorticity at the tip and a cylindrical non-expanding wake. Ramdin [13] showed the Prandtl factor tends to overpredict at 80% blade and underpredict at 95% blade the TL of a free-vortex wake model for Tip-Speed Ratio (TSR) 4 to 10 and five different rotor designs. He attributed these deficiencies to the inability of the model to capture the tip-vortex axial and radial movements and strength variation with TSR and non-uniform high blade loading. Barndlard [12] identified "wake expansion, roll-up, and distortion" as phenomena not included in Prandtl-based factors. By free vortex wake analysis, he also pointed out that TSR, thrust coefficient, and radial distribution of the blade circulation are the governing parameters in decreasing order of importance. Micallef [14, 15] showed by stereo particle image velocimetry and 3D panel method simulations that the last 5-10% blade is affected by radial flow induced by the chordwise bound circulation depending on the tip bluntness, and recommended the inclusion of these effects in the Prandtl model. Characterizing the near-wake and blade tip aerodynamic properties for varying TSR and under non-uniform blade loading is necessary to evaluate the Prandtl factor limitations and its impact on the load distributions and power.

Regarding the inboard blade, the loading increase due to the rotating blade - the so-called Himmleskamp effect [16] - is modeled by SD corrections. Most of them [17–19] modify the 2D airfoil polars according to a correction function obtained from 3D boundary layer analysis. Models differ in the specific definition of this function, but it generally depends on the local chord to radius ratio c/r and empirically derived coefficients. The importance of the c/r ratio was identified by Snel [17] and is related to the radial flow acceleration. Some models [17, 19] correct only the lift coefficient while others correct both lift and drag coefficients [18]. Moreover, the drag coefficient is in some models larger [20] and in others smaller [18] than its 2D value and this remains an unsolved issue [21]. A review of SD corrections was performed by Breton [5] who reported increasing overpredictions of experimental load distributions and deviations between models with increasing inflow speed. He related these results to the limitations of the underlying boundary layer theory such as the lack of transition and its violation under separation. CFD investigations were performed to further understand the phenomenology of SD, [22, 23]. Guntur [22] performed RANS simulations and found that the radial flow develops also outside the separated region due to the action of the centrifugal force on slow-moving chordwise flow. He also observed that pressure distributions in the separated region do not have zero slope as in the non-rotating case due to radial pumping. Bangga [23] showed that both inviscid and viscous 3D flow effects are responsible for SD and observed that it occurs in presence of separated radial flow only when $c/r > 0.1$. Furthermore, he investigated the role of Coriolis and centrifugal forces by Detached Eddy Simulations and observed that the first is strong close to the separation point and near the wall, while the second dominates the rest of the blade flow. Further CFD-based analysis is required to evaluate if the drag coefficient varies under SD and, if so, how much is the effect on the loading.

The goal of this study is to assess the reported Prandtl factor limitations under high loading and expanding wake and the unclear drag coefficient variation under SD. Unsteady RANS simulations are employed for the assessment and to confirm previous findings concerning the phenomenology of TL and SD. The wind turbine considered is the NREL 5MW rotor [24] and three simulation conditions representative of design and off-design conditions are simulated. The study is limited to steady aligned uniform inflow, blades are considered rigid, and only a state-of-the-art BEMT-based

code is considered.

The paper follows with section III where the rotor specifics and simulation conditions are given. Section IV describes the details of the applied methodology and section V reports the verification of the CFD solution. A characterization of the rotor aerodynamics is done in section VI by means of the CFD results, and the comparison between BEMT and CFD predictions is treated in section VII. Finally, the main results are summarized and guidelines are given in the conclusions.

III. Turbine and simulation condition

The NREL 5MW wind turbine [24] was chosen because it is a widely employed benchmark, it contains an extensive data set, and it has similar rated power and rotor diameter ($D = 126$m) as commissioned onshore turbines in Europe in 2021 [25]. The turbine was simulated as an isolated rotor with rigid blades with zero cone and tilt angles. The 3D blade geometry for the CFD simulations was generated by an in-house code from the design provided in [24] and it features a blunt trailing edge along its whole span. The NACA64 airfoil was modified to have a trailing edge thickness of 0.3% chord to facilitate the generation of the CFD mesh. Furthermore, the blade has a 0.8m tip chord and linear interpolation between the profiles is used to reconstruct the blade surface. The latter was enforced also in between the root cylinder and the DU40 airfoil at a 20% radius to achieve representative geometry of wind turbine blades. Finally, a cylindrical shape rounded on the upstream side was designed for the hub geometry, as no reference could be found.

The NREL 5MW rotor was simulated under uniform, aligned, steady inflow conditions for three values of the TSR λ: $\lambda = 7$, $\lambda = 4$, and $\lambda = 10$, representative of design, high wind-speed and Turbulent Wake State (TWS) conditions respectively. The only parameter changing among the three cases is the inflow speed (i.e. $U = 11.4$m/s, $U = 19.95$m/s, and $U = 7.98$m/s), whereas the rotor speed Ω and blade pitch angle are kept constant and equal to 12.1rpm and 0°. The second and third conditions are not representative of steady-state power production operations, but they show the limitations of TL and SD outside the design condition. Finally, international standard atmospheric sea-level pressure, density, and dynamic viscosity values were employed.

IV. Methodology

A. BEMT model and setup

The employed BEMT solution is part of the Simcenter Samcef solver (version 2022.2) [26] and is based on the classic Glauert-Prandlt's theory [6] equipped with Burton's version [27] of the Prandtl [11] TRL correction and the Buhl's AeroDyn [28] TWS correction. BEMT simulations were set-up in the engineering interface Samcef for Wind Turbines (SWT) [29] by prescribing the blade design properties and airfoil polars in [24] except for the NACA64 profile. As the latter was modified with a blunt trailing edge, new polars were computed with the viscous Xfoil solver for a Reynolds number of 6.6 million and forced transition at the leading edge, consistently with the CFD setup. The polars from the NREL report [24] were considered with and without the SD corrections of Du-Selig [18] expanded by the Eggers' drag treatment [20]. SWT performs linear interpolation of the input polar data sets according to a prescribed thickness distribution, which was obtained from the 3D blade geometry. For each blade, 30 sections were used with a more refined discretization towards the blade tip.

B. CFD model and setup

The incompressible RANS equations were simulated by Simcenter STAR-CCM+ (version 2021.2) [30] by both steady-state and unsteady approaches. The k-ω SST turbulence model [31] was employed, as in [32–34], and combined with the Reichhardt [35] hybrid velocity wall function without modeling laminar to turbulent boundary layer transition. The segregated flow solver was selected, with a constant density gas model, and second-order space and time discretization. In the unsteady simulations, a time step corresponding to a 4° rotation angle was selected with 20 internal iterations and at least 8 revolutions were simulated for a sufficient near-wake development. The rotor motion was modeled by the Multiple Reference Frame (MRF) approach in steady-state and rigid-body rotation under unsteady conditions. The MRF approach was implemented by assigning the rotor cylinder region in fig. 1-right of the CFD domain to a rotating frame and the remaining CFD domain in fig. 1-left to a stationary one with an in-plane conformal interface in between the two regions.

To set up the CFD simulations, a similar approach as Dose [32] was followed. As shown in fig. 1, the far-field boundaries were located at 10 and 20 (outlet) diameters from the rotor center with assigned velocity inlets and pressure

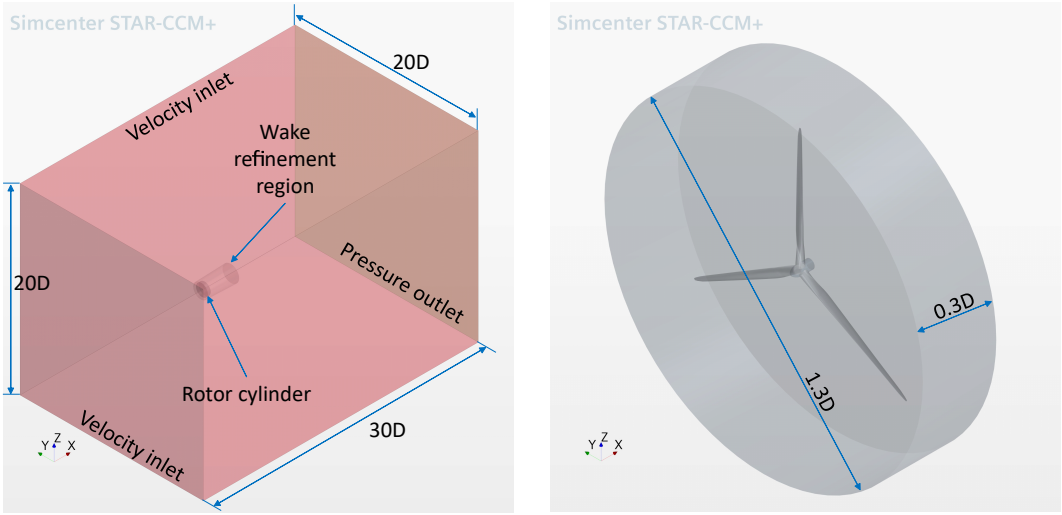

Fig. 1 Regions, sizes, and boundary conditions of the CFD domain. D **refers to the rotor diameter and the reference system displayed is the inertial laboratory one.**

outlet boundary conditions. Moreover, a wake refinement up to 3 diameters downstream was defined. The generated

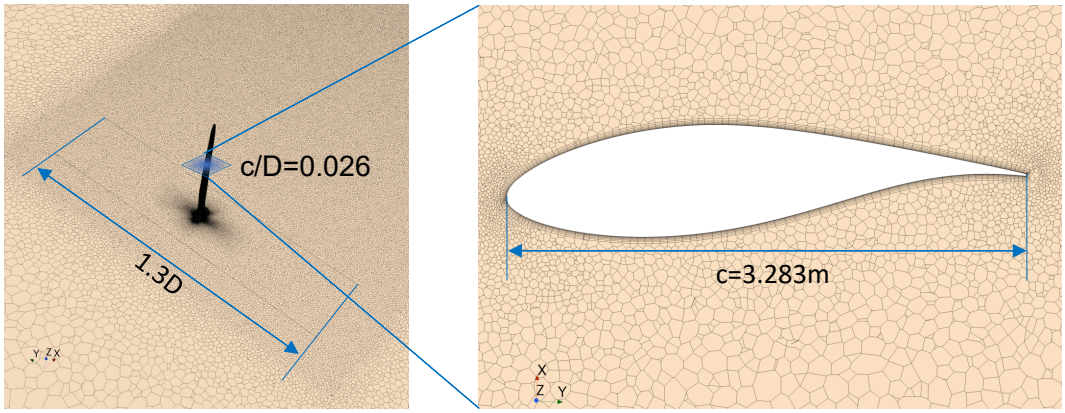

Fig. 2 The "fine" CFD mesh defined in section V: on the left: hub, blade, rotor cylinder region, and wake refinement are shown, on the right: a blade section at 63% radius.

volume mesh was unstructured, as shown in fig. 2, and consisted of polyhedral cells and 8 prismatic layers for the blade boundary layer. The latter had a total of $3.17 \cdot 10^{-4} D$ thickness and achieved a y^+ value in the range 20-300. The cell size was specified constant inside the wake refinement region and on the interface.

C. Post-processing of the CFD solution for the extraction of lifting line variables

The extraction of the inductions, angle of attack, lift and drag coefficients from the rotor CFD simulations was carried out by the Azimuthal-Averaging Technique (AAT) and the inverse BEMT method.

The AAT method computes the annular-averaged axial $\bar{a}$ and tangential $\bar{a'}$ inductions by sampling the near-wake axial U_a and tangential U_t flow velocity components. The method was implemented by using three upstream and three downstream arrays of probes sampling the flow each time step during the last revolution. Probes in each array are organized in 11 annuli from a 20% radius up to the tip with increasing resolution. Probes in each annulus were axially spaced from the rotor center by the local blade chord and contained 90 probes each according to [36]. Next, the sampled velocities were time-averaged at each probe, azimuth-averaged at each annulus, and interpolated at the rotor plane by

Lagrange polynomials as in [33]. Finally, the annular-averaged axial and tangential inductions were computed as:

$$\bar{a} = 1 - \frac{\overline{U_a}}{U} \qquad \bar{a'} = -\frac{\overline{U_t}}{2\Omega r} \tag{1}$$

from the time-azimuth-averaged flow velocities at the rotor plane $\overline{U_a}$ and $\overline{U_t}$.

The inverse BEMT method was implemented consistently with the Samcef BEMT code [26]. The input is the blade out-of-plane F_A and in-plane F_T force density time-averaged over the last revolution. The usage or not of the TRL correction allowed to compute the local and annular-averaged inductions respectively. This is equivalent to the inductions provided by the standard BEMT method with or without the TRL correction and the only difference is the input loading. The local inductions were used to compute the local angle of attack, as explained next. Finally, both inverse BEMT method variations included the Buhl TWS correction [28].

With the annular-averaged $\bar{a}$ $\bar{a'}$ and local a_B a'_B inductions, the corresponding annular-averaged $\bar{\alpha}$ and local α_B angles of attack were computed as:

$$\bar{\alpha} = \arctan\left(\frac{U\left(1-\bar{a}\right)}{\Omega r\left(1+\bar{a'}\right)}\right) - \theta \qquad \alpha_B = \arctan\left(\frac{U\left(1-a_B\right)}{\Omega r\left(1+a'_B\right)}\right) - \theta \tag{2}$$

where θ is the blade twist angle. The local angle of attack α_B was employed to define the downwash angle of attack in the outboard blade. Following [37], the latter can be defined as:

$$\alpha_w = \bar{\alpha} - \alpha_B \tag{3}$$

with α_B provided only by the inverse BEMT method with TRL correction.

Knowledge of the angle of attack and normal c_a and tangential c_t force coefficients allows to compute the lift c_l and drag c_d coefficients from the CFD solution as:

$$c_l = c_a \cos\phi + c_t \sin\phi \qquad c_d = c_a \sin\phi - c_t \cos\phi \tag{4}$$

with $c_a = F_A/(P_{dyn}c)$, $c_t = F_T/(P_{dyn}c)$, $P_{dyn} = 0.5\rho(U^2+(\Omega r)^2)$, and $\phi = \bar{\alpha}+\theta$. The annular-averaged angle of attack considered in the c_l and c_d derivation is just the one provided by the AAT method.

V. Verification of the CFD solution

The CFD solution was assessed by a mesh convergence analysis. Four different grids were simulated by systematically varying a base size for the polyhedral cells, while the prismatic layers were left unmodified to achieve a constant boundary layer resolution, as recommended in [38]. Following [32, 33], only steady-state simulations were performed to reduce the simulation cost and only the rotor thrust and power were considered to assess the mesh convergence.

Figure 3a shows the values of the rotor thrust and power given by the four meshes plotted against the number of mesh cells. The "fine" mesh was selected for the subsequent unsteady simulations, as it is within the discretization uncertainty band of power, and because computationally cheaper than the "very fine" mesh. The "fine" thrust is 750.76kN and the power is 5.384MW. These values were compared with the corresponding ones in [32] obtaining 2.1% thrust and 3.4% power underpredictions. The respective radial distributions of the axial and tangential force densities in the rotor plane are shown in fig. 3b. The differences with the reference distributions primarily involve the outboard blade for thrust, whereas they are spread over a wider blade region from 20 to 80% radius for power. These deviations are due to differences in modeling, possibly in the geometry definition of the blade, mesh topology, and solver. In fig. 3a, the discretization uncertainty band for the rotor power corresponds to a 0.52% discretization error. This was computed by applying the least-square GCI approach in [39] obtaining a Richardson extrapolated value of 5.379MW. The error band is defined with respect to the previous Richardson value. For the rotor thrust, no grid convergence analysis was performed due to the reported oscillatory convergence.

VI. CFD characterization of the rotor aerodynamics

The results from the unsteady RANS simulations obtained with the "fine" mesh are exploited to qualitatively and quantitatively describe the properties of the 3D blade and rotor near-wake aerodynamics.

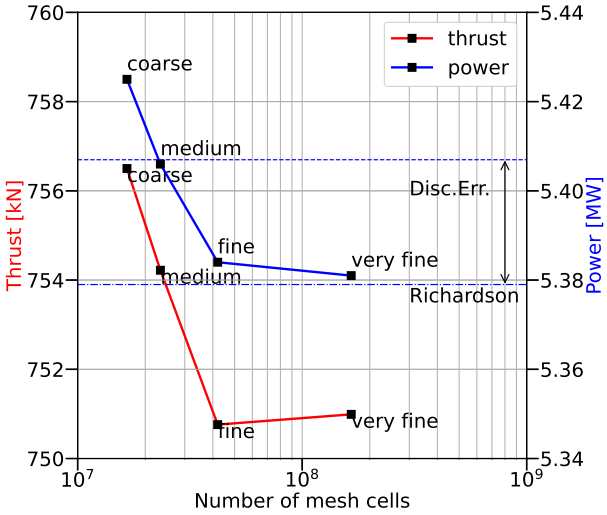

(a) Sensitivity of the rotor thrust and power to the CFD mesh resolution.

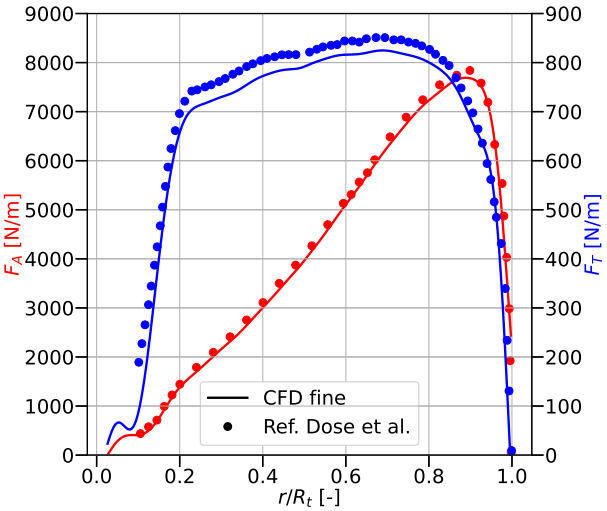

(b) Blade axial and tangential load density distributions for the "fine" mesh and the reference solution [32].

Fig. 3 Results of the CFD mesh convergence study.

The instantaneous flow streamlines over the blade suction surface are shown in fig. 4 and reveal relevant flow features for the three conditions studied. The flow in the mid-inboard blade and near the tip is 3D with a different extent depending on the TSR λ. Near the tip beyond the 90% blade, the flow streamlines bend radially towards the inboard blade and this accentuates for decreasing λ, and the flow is separated close to the trailing edge for $\lambda=4$. Such a radial flow at the blade tip is related to the generation of the tip-vortices and is due to the radial pressure gradient responsible for the pressure equalization between the two sides of the blade surface [40, 41]. In the inboard region and at low

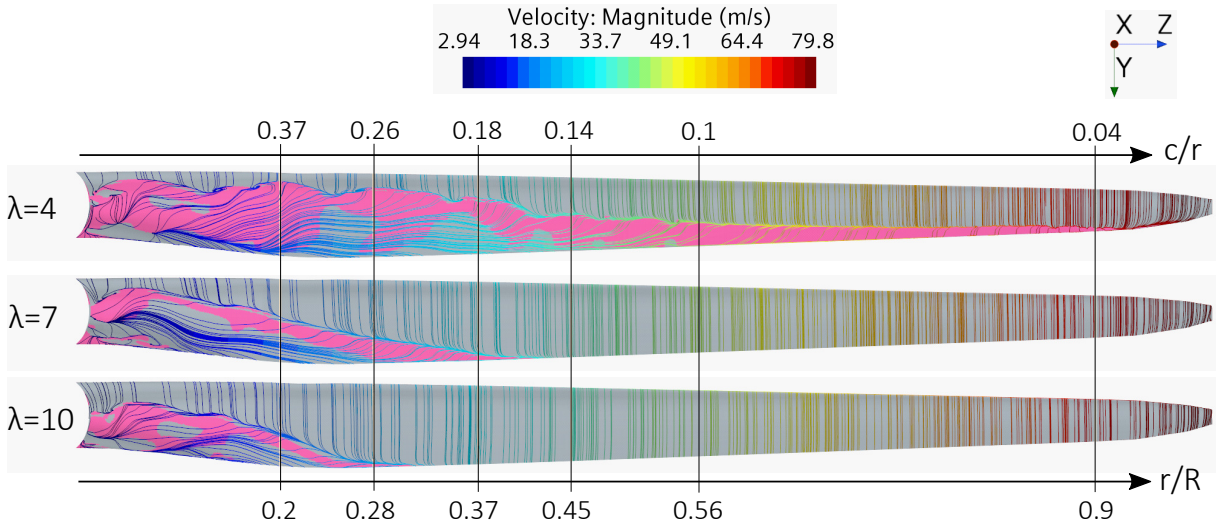

Fig. 4 Instantaneous blade surface streamlines colored by velocity magnitude in the inertial frame as they are seen from a downwind observer. The figure depicts also areas of flow separation with a zero or negative chordwise skin-friction coefficient according to [22]. Five radial locations r/R are shown with the corresponding values of the c/r parameter used in SD corrections.

λ, the blade features limited chordwise-oriented attached flow near the leading edge, while this is more extensive in the midboard blade and for increasing λ. Moving towards the trailing edge, the flow acquires an increasing spanwise component before separating, as observed in [22]. Beyond the separation line, the flow is clearly radial but there are

regions where it reattaches, namely at 20% blade for $\lambda=7$ and 10, and regions where it stays separated, in particular at $\lambda=4$. Reattachment regions occur close to the maximum chord and at high λ, and previous studies [5, 22, 42] related this phenomenon to the root-vortex induction. In the separated regions for $\lambda=4$ and close to the separation line, the Coriolis force was shown to be strong [23] indicating the presence of SD. Finally, beyond 56% blade, the flow is separated only near the trailing edge for $\lambda=4$ and with a limited radial component consistently with the alleviation of SD corrections for $c/r<0.1$.

To quantify the surface flow in the inboard blade, the profiles distributions of the pressure coefficient c_p, chordwise-oriented skin-friction coefficient c_{f_c}, and radial-oriented skin-friction coefficient c_{f_r} are shown in fig. 5 at two radial locations. The pressure distributions reveal a constant-slope region up to the trailing edge covering 70-80% of the

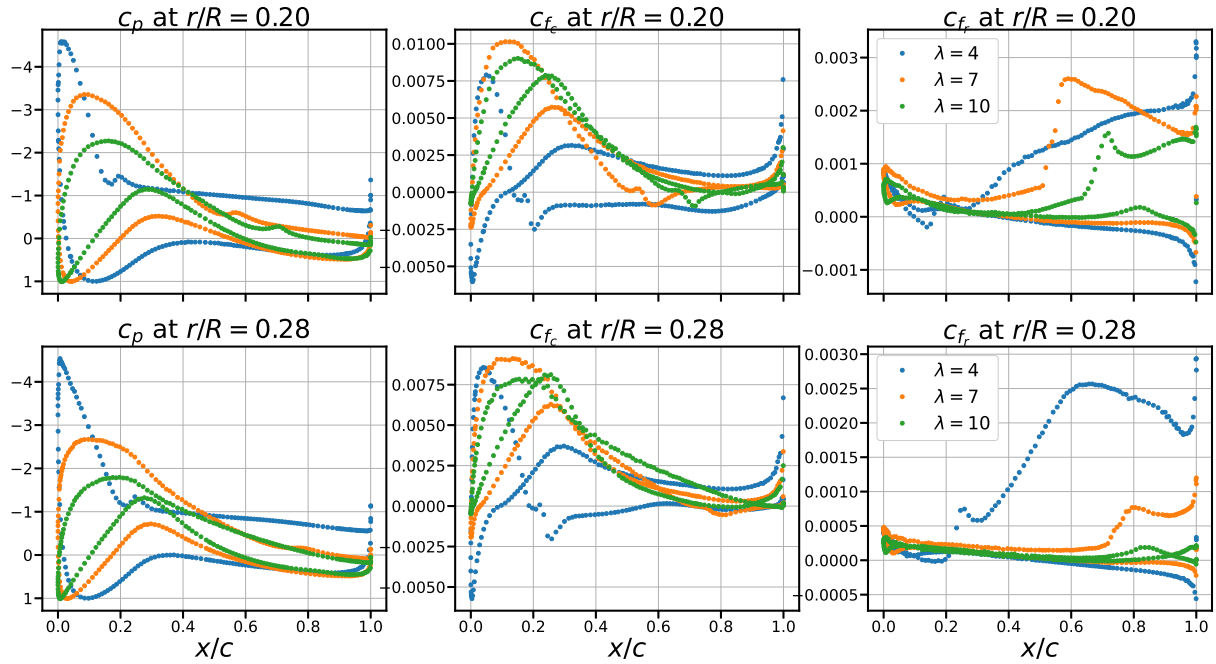

Fig. 5 Pressure c_p, chordwise c_{f_c}, and radial c_{f_r} skin-friction coefficients on the inboard blade profiles. The velocity used in the normalization dynamic pressure includes both the blade profile peripheral velocity Ωr and inflow velocity U.

profile for $\lambda=4$. The chordwise c_f distributions show a large separation region at this condition spanning the entire constant pressure gradient. For larger TSR, the c_{f_c} is slightly negative only around 60-80% chord corresponding to the small separated regions in fig. 4 and the related c_p distributions do not show a constant-slope region. The positive radial c_f region extends over the same separation and constant pressure gradient regions previously observed for $\lambda=4$. Furthermore, the c_{f_r} values at this TSR are larger than the other, especially at 28% blade. Such a relation was identified in [22, 23] as being dominated by the centrifugal and Coriolis forces suggesting a stronger delay of stall for $\lambda=4$ compared to $\lambda=7$ and 10 at these radial locations.

The curved surface streamlines on the outboard blade in fig. 4 are the footprint of the tip-vortices. These and the root-vortices are visualized in fig. 6 for the rotor near-wake up to one diameter downstream. The axial spacing along the x-direction between the tip-vortices increases for reducing λ due to the faster downstream convection of the vortices, which is proportional to the inflow speed. Furthermore, the expansion of the tip-vortices along the radial direction (y- or z-axis) increases for increasing λ. The latter is related to the rotor thrust coefficient increase with λ for zero blade pitch, which correlates with an increase in wake expansion [43]. Momentum theory can be used to model this phenomenon for the $\lambda=4$ and 7, but at $\lambda=10$ the rotor is in a TWS condition, as the rapid breakdown and mixing of the tip-vortices in fig. 6 shows. The root-vortex size increases by reducing λ consistently with the more extensive flow separation on the blade producing large-scale shed vorticity.

The tip-vortex axial and radial displacements can be quantified by tracking the paths of the vortex centers on the X-Z plane in fig. 6 with respect to the tip location of the vertical blade. This is shown in fig. 7-right combined with the pitch of the tip-vortex helix normalized by the rotor radius. The latter increases for reducing λ as reported also by

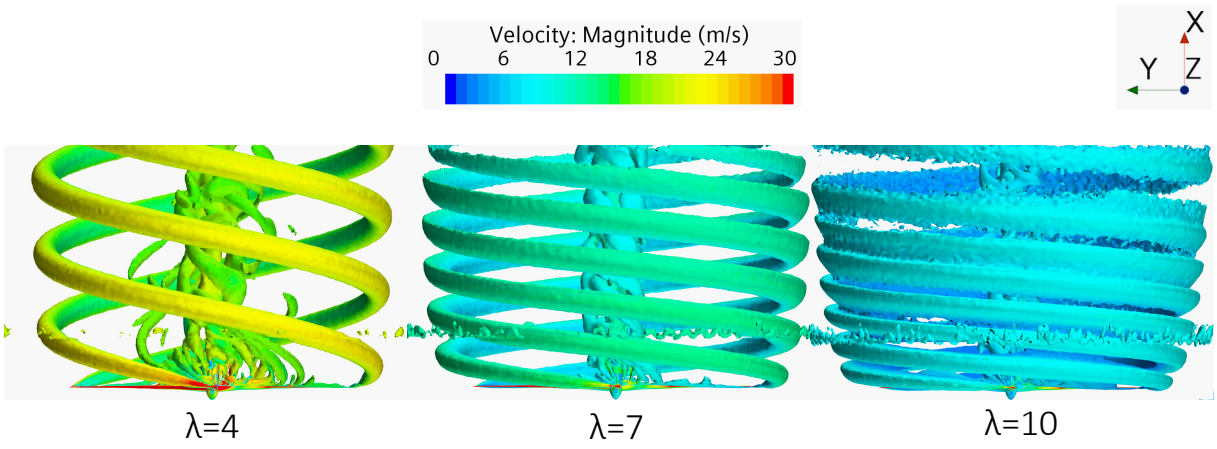

Fig. 6 Vortex structures in the rotor near-wake visualized by an isosurface of the Q-criterion colored by velocity magnitude.

Haans [43]. Furthermore, an increase in wake expansion is observed in terms of a larger z-wise radial distance between the first two vortices for increasing λ, while the radial distance between the subsequent vortices reduces regardless of the TSR. Figure 7-left depicts an estimate of the tip-vortex strength in terms of normalized circulation for various vortex

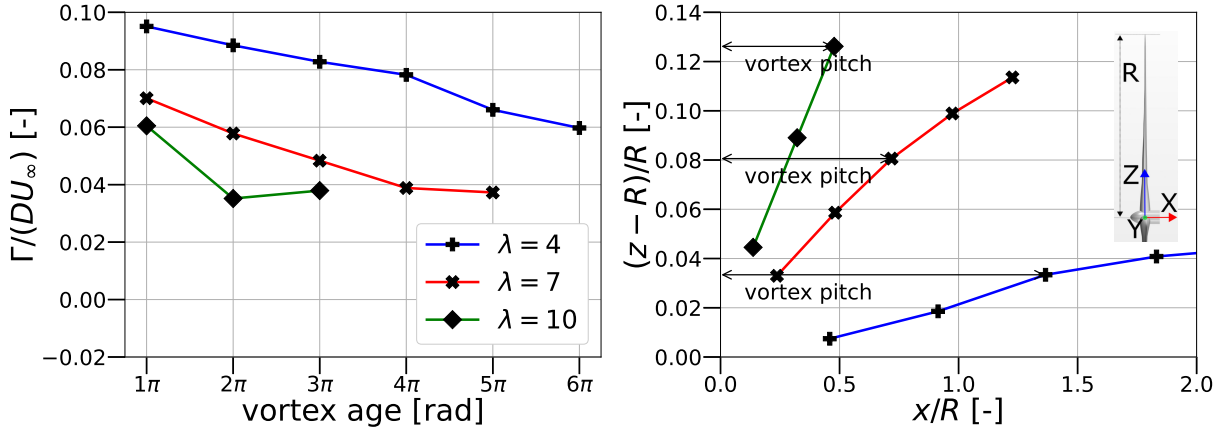

Fig. 7 Centers' trajectories (right) and normalized circulation (left) of the tip-vortices for the three CFD simulation cases. The latter was obtained by surface integration of the vorticity component ω_j sampled on the X-Z plane shown in fig. 6.

ages. It is shown that the lower λ the larger the circulation of the tip-vortex, as observed also by Lignarolo [44]. This can be related to the extent of spanwise flow on the blade tip surface streamlines in fig. 4, which amplifies with reducing λ. The significant (up to 50%) circulation decrease for increasing vortex age is not expected for the coherent tip-vortices before their break-down. As reported in [10], this can be explained by the numerical diffusion of the second-order discretization scheme in the URANS simulations and the 1m cell size in the wake refinement region, despite the grid convergence on the loading observed in section V.

VII. Comparison and discussion of BEMT and CFD predictions

Figure 8 shows the error percentage difference between four BEMT versions and the URANS CFD solution of the rotor thrust and power coefficients for the three simulation conditions. At the high wind speed $\lambda=4$, all BEMT versions significantly underpredict the CFD thrust coefficient up to 25% and power coefficient by 30%. A more favorable match is found at the rated $\lambda=7$ case with an error below 5%, while at the TWS conditions $\lambda=10$ one the error is below 10%. Including the SD correction at $\lambda=4$ improves the thrust coefficient prediction by 10% and the power coefficient one by

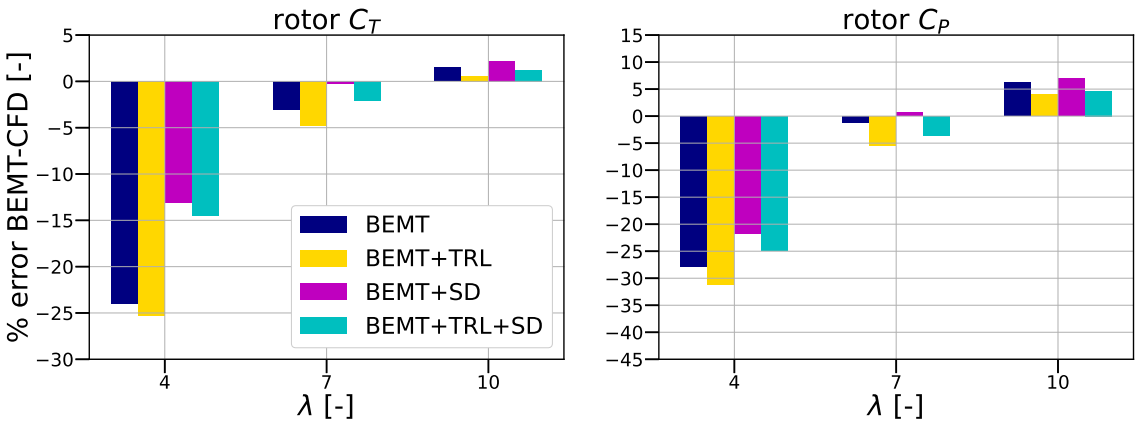

Fig. 8 Errors between BEMT versions and the CFD for the integral rotor thrust and power coefficients versus the TSR λ. The CFD values are obtained by applying their definition to the spanwise integrated thrust F_A and tangential F_T blade force densities averaged over the last revolution. The four BEMT versions are obtained by adding the SD and TRL corrections to the Glauert's BEMT model corrected for TWS (BEMT).

5%. The TRL contribution is below 5% and it leads to better power and worse thrust coefficient predictions for $\lambda > 7$. Overall, BEMT predictions of the rotor power and thrust coefficients are below 5% only at the design TSR, while under off-design conditions they are not as satisfactory. In particular at low λ the error increases up to 30% when the 3D blade aerodynamic effects involve a large blade span.

In fig. 9, the radial distributions of the annular thrust and power coefficients:

$$C_T = \frac{3F_A}{\pi r \rho U^2} \qquad C_P = \frac{3F_T \Omega}{\pi r \rho U^3} \tag{5}$$

are shown to visualize the rotor regions where the aerodynamic models diverge. Substantial differences can be noticed over the whole span depending on the operational condition and these are analyzed in the remainder of this section.

From 20% to 40% radius in the inboard blade, the effect of the SD correction is dominant at $\lambda = 4$. This is consistent with the strong spanwise separated flow and the corresponding constant c_p slope region observed in fig. 5. In fig. 9 a good match with the CFD C_T distribution is achieved at $\lambda = 4$, but not an equally satisfactory one for the C_P. The latter is due to an overestimation by more than a factor 2 of the drag coefficient c_d by the SD correction, as shown in fig. 10. The underlying tangential force density expression according to the BEMT theory is:

$$F_T = \frac{1}{2}\rho U_{rel}^2 c (c_l \sin\phi - c_d \cos\phi) \tag{6}$$

where U_{rel} is the local inflow speed. F_T reduces for increasing c_d despite the large inflow angles ϕ experienced in the inboard blade for high U. This results in a C_P underestimation. As already discussed, the c_d treatment is an unsolved problem in the modeling of SD. Furthermore, this was shown to be blade-dependent: the NREL Phase VI turbine showed an increase in 3D c_d [5], while Bangga [23] predicted a decrease in the inboard blade for the AVATAR turbine by DES simulations. Results in fig. 10 provide lower c_d compared to the corrected and uncorrected BEMT versions for SD. The computation of the chordwise c_f and c_p distributions for the 2D blade profiles by RANS simulations is deemed necessary to evaluate the effect of the SD on the drag coefficient.

In fig. 9 and in the inboard blade for $\lambda = 7$ and 10, both BEMT versions overpredict the C_T and C_P distributions by 20%. At the rated TSR the SD correction is active up to a 30% radius, while at the TWS condition it has a negligible contribution. It was observed in section VI that the blade aerodynamics at both conditions is characterized by limited separated spanwise flow with rotational augmentation, while most of the radial flow was attached around 20% blade due to the root-vortex induction. The latter leads to the downwash effect visible in fig. 11 as a reduction of the CFD c_l for $\lambda = 10$ compared with the BEMT polars, which are unaffected by SD due to the low angle of attack. The downwash effect was observed in previous CFD simulations and wind tunnel experiments [5, 22, 42] and this study shows that it is responsible for deviations in load distributions between BEMT-based codes and CFD. Therefore, the root-vortex downwash at a low angle of attack should be accounted for by extending SD corrections, correcting 2D airfoil polars with a dedicated model, or by enforcing the Prandtl Root-Loss (RL) factor in the region of the maximum chord.

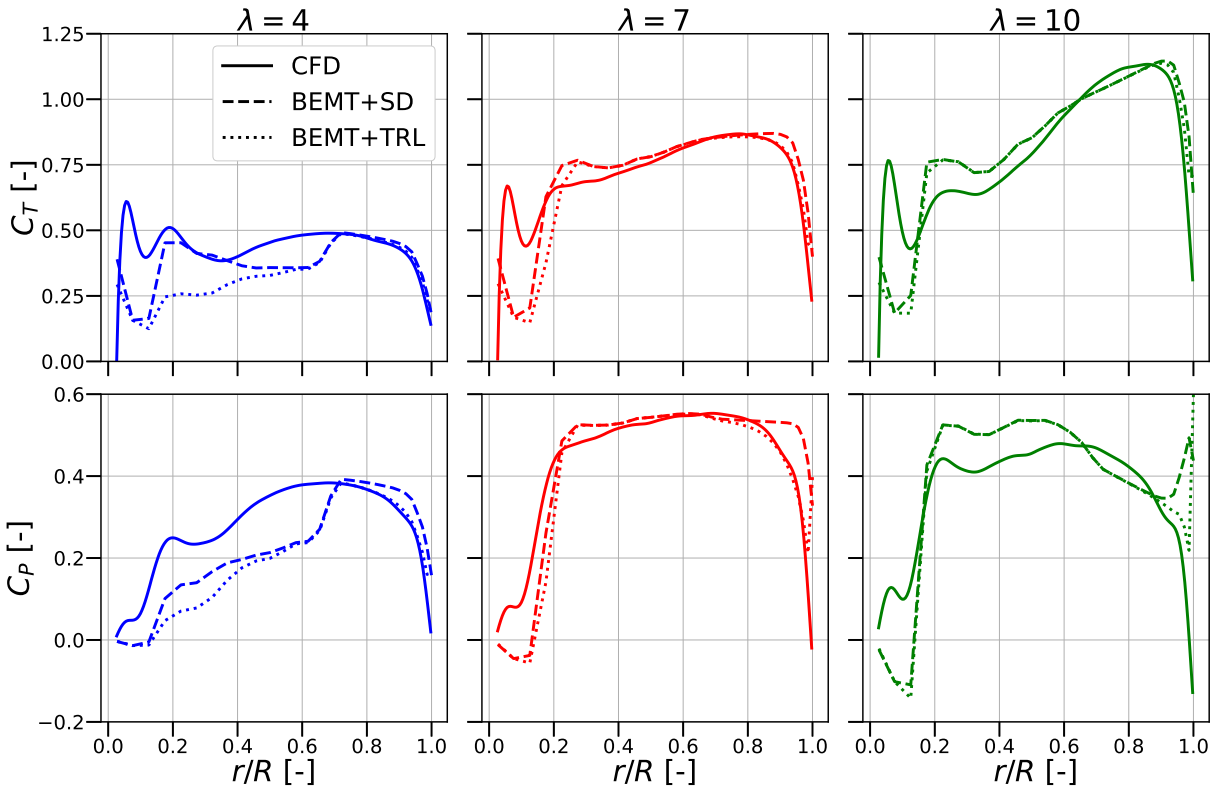

Fig. 9 Annular thrust C_T and power C_P coefficient distributions for the CFD solution, the overall best (BEMT+SD), and overall worst (BEMT+TRL) BEMT versions based on fig. 8 results against the rotor non-dimensional radius.

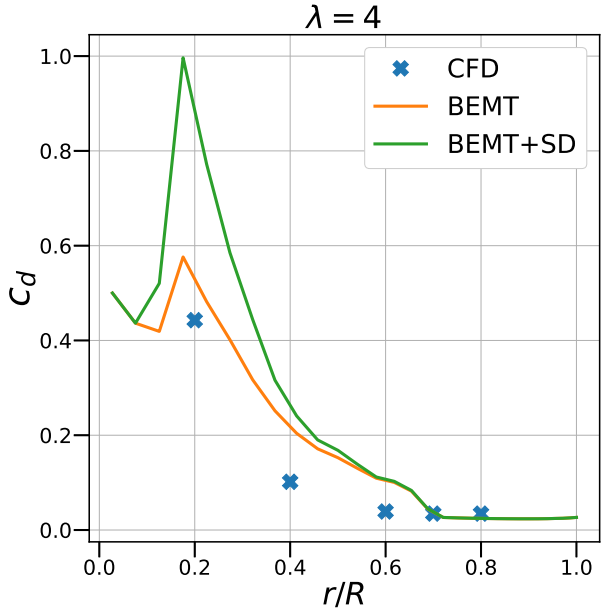

Fig. 10 Radial distributions of the drag coefficient c_d at $\lambda = 4$ as defined in eq. (4) and obtained as described in section IV.

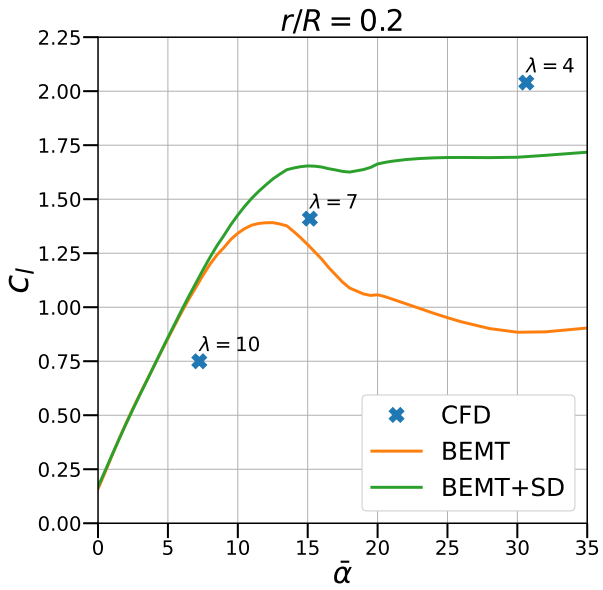

Fig. 11 Lift coefficient c_l polars at a 20% radius computed by BEMT with and without SD correction and extracted from the CFD simulations. The latter was obtained as in fig. 10.

The C_T and C_P distributions in fig. 9 show that for $r/R > 0.7$ the effect of the TRL correction is dominant. This is particularly true for the C_P distribution and the Prandtl factor positively affects the accuracy of BEMT distributions at $\lambda = 4$ and 7 for both quantities. However, at high λ, the TRL correction overestimates the C_T and C_P over the last 10% blade by 5 to 15%. These observations can be explained by looking at the tip-vortex properties from the CFD solution in fig. 7 and the downwash angle of attack α_w which represents the tip-vortex induction. Figure 7-right shows that the

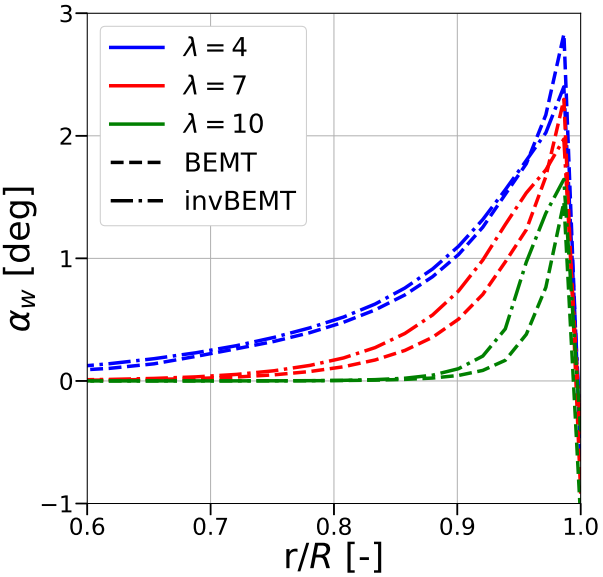

Fig. 12 Downwash angle of attack distributions in the outboard blade according to the BEMT and inverse BEMT methods. The underlying local and annular-averaged angles of attack were obtained for the two approaches as described in section IV.

first tip-vortex, which dominates the downwash effect, has a much higher distance in the X-Z plane from the blade tip at $\lambda = 4$ compared to $\lambda = 10$, because of the order of magnitude difference between its X and Z components. Furthermore,

in fig. 7-left the first tip-vortex at $\lambda=4$ has a stronger circulation. This means that at $\lambda=4$ the tip downwash effect covers a larger portion of the outboard blade region: 40 vs 10% blade, as the α_w plot shows. Differently, at $\lambda=10$ the first tip-vortex induction is concentrated on the last 10% blade, as shown by the rapid downwash increase in fig. 12. Another observation is that BEMT and the inverse BEMT α_w distributions deviate for increasing λ. This is due to: (1) the CFD load contains the tip-vortex induction compared to the BEMT polars, (2) the Prandtl factor cylindrical wake assumption is not consistent with the expanding near-wake at high TSR. Further investigations of the tip downwash effect under TWS conditions are required by a method able to extract the local inductions from the CFD near-wake solution.

The difference between BEMT and CFD predictions is not only related to the modeling of 3D SD and TL. As shows in fig. 8, BEMT versions corrected for SD and TRL provided around 15% deviation with the CFD rotor thrust and power coefficients at $\lambda=4$, an error about 2 to 3 times larger than at $\lambda=10$ and 7. Furthermore, such a deviation is concentrated below 15% radius in the root region and around 60% in the midboard blade according to the related distributions in fig. 9. In the root region, BEMT versions underestimate by a factor of 2 to 3 the C_T and C_P distributions

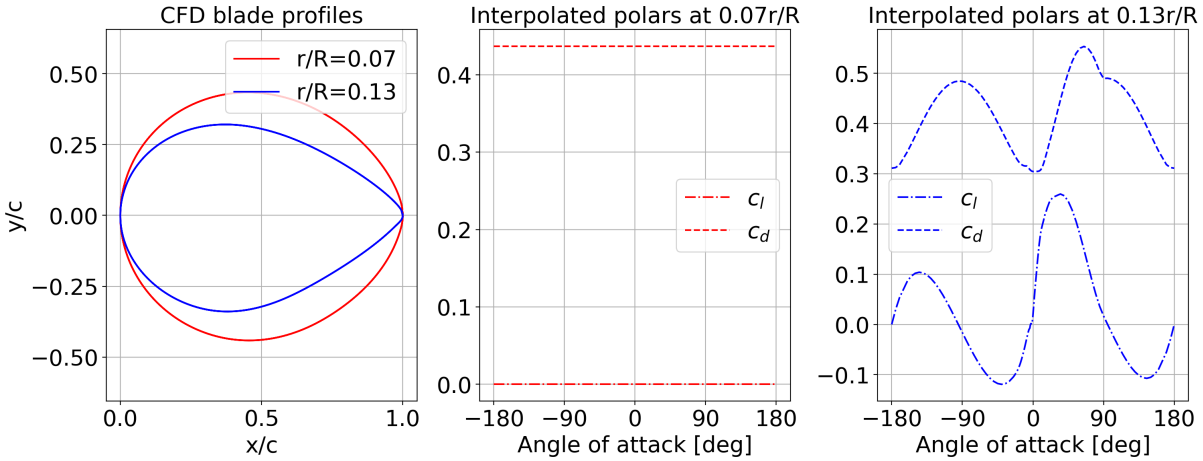

Fig. 13 Profiles in the root region of the CFD blade and the corresponding linearly interpolated lift c_l and drag c_d coefficient polars used in the BEMT simulations.

at all TSR, not just at $\lambda=4$. This is due to the polars shown in fig. 13, which were obtained by linear interpolation between the constant c_d polar of the cylindrical profile and those of the DU40 airfoil. Despite this approach is consistent with the CFD blade geometry generation described in section III, such polars do not represent the 3D, largely separated, and rotationally augmented flow ($c/r \gg 0.1$) over these profiles discussed in section VI. In the midboard blade, there is a clear mismatch between aerodynamic models only at $\lambda=4$. The underlying reason is the different CFD and BEMT c_l and c_d polars of the DU21 airfoil under separation, as shown in fig. 14. The firsts predict limited separation with the lift coefficient still rising, while the seconds are experimentally derived and predict a post-stall condition. Similar observations were reported in [45] by 2D RANS, which are comparable to 3D RANS due to the negligible SD effects at 60% blade and $\lambda=4$. Furthermore, Bertagnolio [45] observed that transition is an important aspect to improve the match with the experimental polars for profiles with around 20% thickness-to-chord ratio, sharp suction peak, and low-pressure gradient, such as the DU21. Therefore, airfoil polars are at least as important as corrections at low TSR for the accuracy of load predictions. It is recommended to exploit CFD simulations to obtain polars representative of the aerodynamics of the root profiles with thickness greater than 40% chord. Concerning the CFD simulation, further work is necessary to assess the effect of transition, combined with wall-resolved or turbulent scale resolving simulations, to validate RANS predictions at $\lambda=4$.

VIII. Conclusions

In this study, an industrial BEMT-based code was scrutinized by comparison with URANS simulations for the prediction of load distributions and power. The comparison focused on design and off-design conditions under uniform aligned steady inflow, and involved the NREL 5MW wind turbine rotor with rigid blades. In accordance with previous literature, it is confirmed that BEMT-based codes cannot accurately predict the URANS rotor thrust and power coefficients at off-design conditions. In particular, at a TSR of 4, the error is up to 30%. These deviations are due to

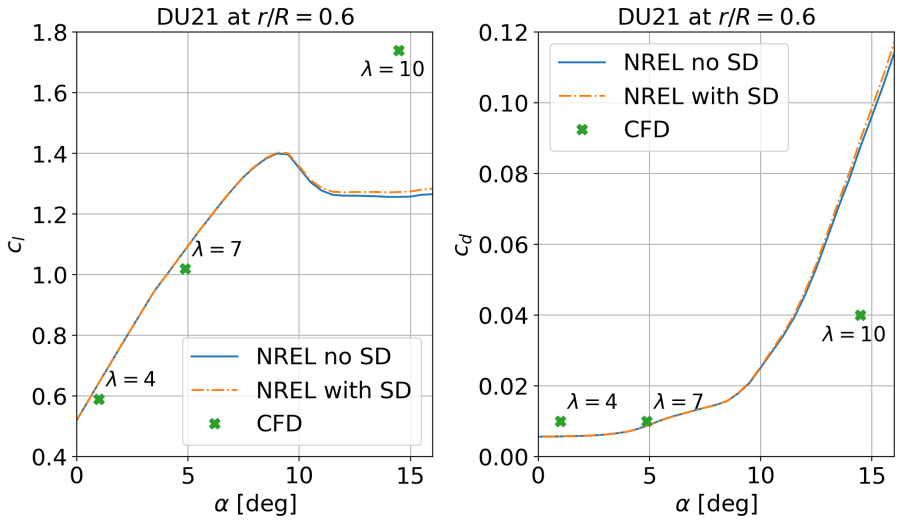

Fig. 14 DU21 lift c_l and drag c_d coefficient polars from the NREL report with and without SD corrections as used in the BEMT simulations and extracted from the CFD solutions as explained in section IV.

limitations of SD and TRL corrections for the 3D aerodynamic phenomena experienced in the inboard and outboard blade. More in detail, the following is reported:

- The Eggers SD correction overpredicts the CFD drag coefficient in the inboard blade at a TSR of 4 by more than a factor of 2. RANS simulations of both 3D blades and 2D profiles are needed to further quantify rotational augmentation effects on the drag coefficient.
- BEMT overestimates load distributions in the inboard blade at a TSR of 10 by 20% due to the unaccounted root-vortex downwash. It is recommended to extend SD corrections to angles of attack below the stall value or to adjust the Prandtl RL correction to the radial location of the maximum chord in order to capture this phenomenon.
- The Prandtl TL factor is challenged at a high TSR because it does not model wake expansion. This provides 5 to 15% larger loads on the last 10% blade. Further studies should: (1) employ methods that can extract the local lifting-line variables from the CFD near-wake solution, (2) investigate the interaction between TL and TWS corrections in BEMT-based codes.

Finally, it was observed that polar data are at least as important as the stall delay correction at a low TSR. This involves both the root region and the midboard blade under 2D separation. Efforts should be made to extract polars from experimental or CFD simulations of profiles with more than 40% thickness-to-chord ratios.

Acknowledgments

The CFD simulations were performed in the HPC12 cluster of the Delft University of Technology (Netherlands). The blade geometry for CFD simulations was obtained from a computer program developed by Prof. Alberto Cardona's research group of the Universidad Nacional del Litoral in Santa Fe (Argentina). The work was funded by the European Research Council within the European Union's Horizon 2020 research and innovation programme under grant agreement N.860101.

References

[1] Thé, J., and Yu, H., "A critical review on the simulations of wind turbine aerodynamics focusing on hybrid RANS-LES methods," *Energy*, Vol. 138, 2017, pp. 257–289. https://doi.org/10.1016/j.energy.2017.07.028.

[2] Veers, P., Dykes, K., Lantz, E., Barth, S., Bottasso, C. L., Carlson, O., Clifton, A., Green, J., Green, P., Holttinen, H., Laird, D., Lehtomäki, V., Lundquist, J. K., Manwell, J., Marquis, M., Meneveau, C., Moriarty, P., Munduate, X., Muskulus, M., Naughton, J., Pao, L., Paquette, J., Peinke, J., Robertson, A., Sanz Rodrigo, J., Sempreviva, A. M., Smith, J. C., Tuohy, A., and Wiser, R., "Grand challenges in the science of wind energy," *Science*, Vol. 366, No. 6464, 2019, p. eaau2027. https://doi.org/10.1126/science.aau2027.

[3] Hansen, M. O. L., and Aagaard Madsen, H., "Review Paper on Wind Turbine Aerodynamics," *Journal of Fluids Engineering*, Vol. 133, No. 11, 2011. https://doi.org/10.1115/1.4005031.

[4] Schepers, J., Boorsma, K., Cho, T., Gomez-Iradi, S., Schaffarczyk, P., Shen, W., Lutz, T., Stoevesandt, B., Schreck, S., Micallef, D., Pereira, R., Madsen, H., and Sørensen, N., "Final report of IEA Task 29, Mexnext (Phase 1): analysis of Mexico wind tunnel measurements." Report ECN-E–12-004, Energy Research Council of the Netherlands, 2012.

[5] Breton, S. P., Coton, F. N., and Moe, G., "A study on rotational effects and different stall delay models using a prescribed wake vortex scheme and NREL phase VI experiment data," *Wind Energy*, Vol. 11, No. 5, 2008, pp. 459–482. https://doi.org/10.1002/we.269.

[6] Glauert, H., *Airplane Propellers*, Springer Berlin Heidelberg, 1935, pp. 169–360. https://doi.org/10.1007/978-3-642-91487-4_3.

[7] Hansen, M. O. L., Sørensen, J. N., Voutsinas, S., Sørensen, N., and Madsen, H. A., "State of the art in wind turbine aerodynamics and aeroelasticity," *Progress in Aerospace Sciences*, Vol. 42, No. 4, 2006, pp. 285–330. https://doi.org/10.1016/j.paerosci.2006.10.002.

[8] Wang, L., Liu, X., and Kolios, A., "State of the art in the aeroelasticity of wind turbine blades: Aeroelastic modelling," *Renewable and Sustainable Energy Reviews*, Vol. 64, 2016, pp. 195–210. https://doi.org/10.1016/j.rser.2016.06.007.

[9] Simms, D., Schreck, S., Hand, M., and Fingersh, L., "NREL Unsteady Aerodynamics Experiment in the NASA-Ames Wind Tunnel: A Comparison of Predictions to Measurements," Report NREL/TP-500-29494, National Renewable Energy Laboratory, 2001.

[10] Boorsma, K., Schepers, J. G., Gomez-Iradi, S., Herraez, I., Lutz, T., Oggiano, L., Pirrung, G., Madsen, H. A., Shen, W., Rahimi, H., and Schaffarczyk, P., "Final report of IEA Task 29, Mexnext (Phase 3)," Report ECN-E-18-003, Energy Research Council of the Netherlands, 2018.

[11] Prandtl, L., "Applications of modern hydrodynamics to aeronautics," Report No. 116, NACA, 1921.

[12] Branlard, E., Dixon, K., and Gaunaa, M., "Vortex methods to answer the need for improved understanding and modelling of tip-loss factors," *IET Renewable Power Generation*, Vol. 7, No. 4, 2013, pp. 311–320. https://doi.org/https://doi.org/10.1049/iet-rpg.2012.0283.

[13] Ramdin, S., "Prandtl tip loss factor assessed," MSc Thesis, Delft University of Technology, 2017.

[14] Micallef, D., "3D flows near a HAWT rotor: A dissection of blade and wake contributions," Ph.D. Thesis, Delft University of Technology, 2012.

[15] Micallef, D., Akay, B., Ferreira, C. S., Sant, T., and van Bussel, G., "The origins of a wind turbine tip vortex," *Journal of Physics: Conference Series*, Vol. 555, 2014, p. 012074. https://doi.org/10.1088/1742-6596/555/1/012074.

[16] Himmelskamp, H., "Profile investigations on a rotating airscrew," Ph.D. Thesis, University of Goettingen, 1945.

[17] Snel, H., Houwink, R., and Piers, W. J., "Sectional Prediction of 3D Effects for Separated Flow on rotating blades," *18th European Rotorcraft Forum Avignon France*, 1992, pp. 15–18.

[18] Du, Z., and Selig, M., "A 3-D stall-delay model for horizontal axis wind turbine performance prediction," *1998 ASME Wind Energy Symposium*, 1998. https://doi.org/10.2514/6.1998-21.

[19] Dumitrescu, H., and Cardos, V., "Inboard Stall Delay due to Rotation," *Journal of Aircraft*, Vol. 49, No. 1, 2012, pp. 101–107. https://doi.org/10.2514/1.C031329.

[20] Eggers, A., Chaney, K., and Digumarthi, R., "An Assessment of Approximate Modeling of Aerodynamic Loads on the UAE Rotor," *41st Aerospace Sciences Meeting and Exhibit*, 2003. https://doi.org/10.2514/6.2003-868.

[21] Burgos Tafur, B. S., Daniele, E., Stoevesandt, B., and Thomas, P., "On the calibration of rotational augmentation models for wind turbine load estimation by means of CFD simulations," *Acta Mechanica Sinica*, Vol. 36, No. 2, 2020, pp. 306–319. https://doi.org/10.1007/s10409-020-00949-0.

[22] Guntur, S., "A detailed study of the rotational augmentation and dynamic stall phenomena for wind turbines," Ph.D. Thesis, Technical University of Denmark, 2013.

[23] Bangga, G., "Three-dimensional flow in the root region of wind turbine rotors," Ph.D. Thesis, University of Stuttgart, 2018.

[24] Jonkman, J., Butterfield, S., Musial, W., and Scott, G., "Definition of a 5-MW Reference Wind Turbine for Offshore System Development," Report NREL/TP-500-38060, National Renewable Energy Laboratory, 2009.

[25] Komusanac, I., Brindley, G., Fraile, D., and Ramirez, L., "Wind energy in Europe. 2021 Statistics and the outlook for 2022-2026," Report, Wind Europe, 2021.

[26] "Simcenter Samcef version 2022.2 User Manual," Siemens Digital Industries Software, 2021.

[27] Burton, T., Jenkins, N., Sharpe, D., and Bossanyi, E., *Wind Energy Handbook*, 2nd ed., John Wiley and Sons, 2011. https://doi.org/doi:10.1002/9781119992714.

[28] Buhl, M. L., "A New Empirical Relationship between Thrust Coefficient and Induction Factor for the Turbulent Windmill State," Report NREL/TP-500-36834, National Renewable Energy Laboratory, 2005.

[29] "Samcef for Wind Turbines version 2020.1 User Documentation," Siemens Digital Industries Software, 2020.

[30] "Simcenter STAR-CCM+ version 2021.3 User Guide," Siemens Digital Industries Software, 2021.

[31] Menter, F., "Two-equation eddy-viscosity turbulence models for engineering applications," *AIAA journal*, Vol. 32, No. 8, 1994, pp. 1598–1605.

[32] Dose, B., Rahimi, H., Herráez, I., Stoevesandt, B., and Peinke, J., "Fluid-structure coupled computations of the NREL 5MW wind turbine by means of CFD," *Renewable Energy*, Vol. 129, 2018, pp. 591–605. https://doi.org/10.1016/j.renene.2018.05.064.

[33] Guntur, S., and Sørensen, N. N., "An evaluation of several methods of determining the local angle of attack on wind turbine blades," *Journal of Physics: Conference Series*, Vol. 555, 2014, p. 012045. https://doi.org/10.1088/1742-6596/555/1/012045.

[34] Bangga, G., "Comparison of Blade Element Method and CFD Simulations of a 10 MW Wind Turbine," *Fluids*, Vol. 3, No. 4, 2018. https://doi.org/10.3390/fluids3040073.

[35] Reichardt, H., "Vollständige Darstellung der turbulenten Geschwindigkeitsverteilung in glatten Leitungen," *ZAMM-Journal of Applied Mathematics and Mechanics/Zeitschrift für Angewandte Mathematik und Mechanik*, Vol. 31, No. 7, 1951, pp. 208–219.

[36] Rahimi, H., Schepers, J. G., Shen, W. Z., García, N. R., Schneider, M. S., Micallef, D., Ferreira, C. J. S., Jost, E., Klein, L., and Herráez, I., "Evaluation of different methods for determining the angle of attack on wind turbine blades with CFD results under axial inflow conditions," *Renewable Energy*, Vol. 125, 2018, pp. 866–876. https://doi.org/10.1016/j.renene.2018.03.018.

[37] Zhong, W., Shen, W. Z., Wang, T. G., and Zhu, W. J., "A New Method of Determination of the Angle of Attack on Rotating Wind Turbine Blades," *Energies*, Vol. 12, No. 20, 2019. https://doi.org/10.3390/en12204012.

[38] Roache, P. J., "Quantification of uncertainty in computational fluid dynamics," *Annu. Rev. Fluid. Mech.*, Vol. 29, No. 1, 1997, p. 123–60. https://doi.org/https://doi.org/10.1146/annurev.fluid.29.1.123.

[39] Eça, L., and Hoekstra, M., "Discretization Uncertainty Estimation based on a Least version of the Grid Convergence Index," *2nd Workshop on CFD Uncertainty Analysis, Lisbon, October 2006*, 2006.

[40] Wimshurst, A., and Willden, R. H. J., "Analysis of a tip correction factor for horizontal axis turbines," *Wind Energy*, Vol. 20, No. 9, 2017, pp. 1515–1528. https://doi.org/10.1002/we.2106.

[41] Wimshurst, A., and Willden, R. H. J., "Computational observations of the tip loss mechanism experienced by horizontal axis rotors," *Wind Energy*, Vol. 21, No. 7, 2018, pp. 544–557. https://doi.org/10.1002/we.2177.

[42] Sørensen, N. N., Michelsen, J. A., and Schreck, S., "Navier–Stokes predictions of the NREL phase VI rotor in the NASA Ames 80 ft × 120 ft wind tunnel," *Wind Energy*, Vol. 5, No. 2-3, 2002, pp. 151–169. https://doi.org/https://doi.org/10.1002/we.64, https://doi.org/10.1002/we.64.

[43] Haans, W., "Wind turbine aerodynamics in yaw: unravelling the measured rotor wake," Ph.D. Thesis, Delft University of Technology, 2011.

[44] Lignarolo, L. E. M., Ragni, D., Krishnaswami, C., Chen, Q., Simão Ferreira, C. J., and van Bussel, G. J. W., "Experimental analysis of the wake of a horizontal-axis wind-turbine model," *Renewable Energy*, Vol. 70, 2014, pp. 31–46. https://doi.org/10.1016/j.renene.2014.01.020.

[45] Bertagnolio, F., Sørensen, N., Johansen, J., and Fuglsang, P., "Wind turbine airfoil catalogue," Report Risoe-R No. 1280(EN), Riso National Laboratory, 2001.